Dislocation reactions dominated pop-in events in nanoindentation of Ni-based single crystal superalloys

Zhiwei Zhang [a,b], Wei Cai [c], Yihui Feng [d], Guihua Duan [d], Jing Wang [d], Jun Wang [d,*], Rong Yang [d], Pan Xiao [d], Fujiu Ke [c], Chunsheng Lu [e,*]

[a] Key Laboratory of Mechanics on Disaster and Environment in Western China Attached to the Ministry of Education of China, Lanzhou University, Lanzhou 730000, Gansu, PR China
[b] Department of Mechanics and Engineering Science, College of Civil Engineering and Mechanics, Lanzhou University, Lanzhou 730000, Gansu, PR China
[c] School of Physics, Beihang University, Beijing 100191, China
[d] State Key Laboratory of Nonlinear Mechanics (LNM), Institute of Mechanics, Chinese Academy of Sciences, Beijing 100190, China
[e] School of Civil and Mechanical Engineering, Curtin University, Perth, WA 6845, Australia

ARTICLE INFO

ABSTRACT

In this paper, from both experimental and atomistic simulation perspectives, we have systematically elaborated on the formation of stacking fault tetrahedrons that induces the pop-in events in Ni-based single crystal superalloys under nanoindentation. The magnitude of a displacement burst is proportional to the number and size of stacking fault tetrahedrons. The external work and strain energy stored in dislocations are further discussed in order to ascertain the energy conversion during pop-in events. The findings can provide new insights into a deep understanding of the pop-in events in Ni-based single crystal superalloys and benefit their wide applications in the aerospace industry.

1. Introduction

Over the past few decades, depth-sensing nanoindentation experimental and numerical technologies have been well developed to obtain the mechanical properties and deformation mechanisms of metallic materials at micro- and nano-meter scales [1–4]. The indentation force- and hardness-depth curves can be utilized to extract the mechanical properties such as average hardness, elastic modulus and adhesion performance. Displacement bursts are usually observed in indentation force-depth curves of a material when indentation depth is less than several tens of nano-meters. This is believed to be an elastic-to-plastic transition, which is also known as "pop-in events" [5–9].

The pop-in events can be classified into two categories in indentation force-depth curves of metallic materials. One is the first pop-in event with a larger magnitude of displacement burst, and the other is subsequent successive pop-in events with smaller displacement excursions [10]. It is shown that pop-in events can be also divided into alternative two categories depending on crystal structures of materials. In the first category, the pop-in event occurs only once (i.e., the so-called single pop-in) in body-centered cubic metals. However, in the second category, several pop-in events take place in face-centered cubic metallic

materials that is referred to the successive pop-in [11–14]. Moreover, pop-in modes are related to the shape of an indenter and crystalline orientation [10,15]. To examine the underlying nature of these pop-in modes, numerous nanoindentation experiments, theoretical analyses and molecular dynamic (MD) simulations have been carried out to ascertain the corresponding intrinsic mechanism in metallic materials [10,11,16–18]. For example, Shibutani et al. [11] explored the pop-in events and their mechanisms in face-centered cubic single crystal materials by experiments, and indicated that these events are related to slip of perfect dislocations and activation of partial dislocations. Xia et al. [10] explained the mechanism of pop-in mode and found that the first pop-in event occurs near a theoretical shear stress and the heterogeneous dislocation nucleation may be responsible for subsequent pop-in events. Furthermore, Zhou et al. [16] investigated the pop-in modes and deformation mechanisms in face- and body-centered cubic structural metals, and their MD simulations showed that the nucleation order of half prismatic dislocation loops is the main reason for different pop-in patterns in these two kinds of crystalline structures. Nevertheless, it is worth noting that most of these studies are focusing on pop-in modes in order to identify predominant deformation mechanisms. Due to the lack of real-time and in-situ experimental results and a visible dislocation

---

* Corresponding authors.
E-mail addresses: wangjun@lnm.imech.ac.cn (J. Wang), c.lu@curtin.edu.au (C. Lu).

evolution technique, there is still not a consensus on the deformation mechanism of pop-in events. Especially, the dislocation evolution during pop-in events remains unexplored.

As is well known, Ni-based single crystal superalloys have been widely used in aeronautic and astronautic industries because of their excellent thermomechanical performance [19–21]. This is mainly attributed to the L1$_2$ Ni$_3$Al precipitated phase, Ni$_3$Al/Ni coherent interfaces, and other doping elements. The presence of Ni$_3$Al/Ni interfacial misfit dislocation network structure is also a favorable factor that can absorb and impede active dislocations in Ni matrix and Ni$_3$Al precipitated phase [22–24]. Thus, Ni-based single crystal superalloys are different from other single crystals in deformation mechanisms [25]. Due to safety concerns, it is vital to investigate the elastic-to-plastic transition and its underlying mechanism in Ni-based single crystal superalloys. Since the elastic-to-plastic transition exactly corresponds to the first pop-in event [5–9], investigation can be performed by nanoindentation. However, it is rather difficult, if not impossible, to experimentally ascertain the mechanism behind pop-in events because of the lack of an in-situ nanoindentation technique with a proper temporal and spatial resolution. Fortunately, such a task can be resorted to MD simulations.

In this paper, a series of nanoindentation experiments and MD indentation simulations are firstly performed in Ni-based single crystal superalloys, with the maximum indentation depths ranging from 50 to 400 nm in testing and 4 nm in the MD model. Especially, pre-existing defects are concerned in the MD model, such as the Ni$_3$Al/Ni interface misfit dislocation network and free surfaces. The interface misfit dislocation network can block and absorb matrix dislocations in Ni-based superalloys and the free surface allows annihilation of dislocations. Therefore, the MD model is much closer to an actual material in comparison with others in literature and thus, it can produce indentation force- and hardness-depth curves that are consistent with that from experiments. Then, pop-in events are investigated at macroscopic and atomistic levels and the corresponding dislocation evolution is visualized. This can help to better reveal the deformation mechanism behind pop-in events of Ni-based single crystal superalloys. After that, an energy conversion model is constructed to reveal the underlying mechanism through the energy conversion between external work and strain energy stored in dislocations during pop-in events. Finally, the magnitudes of displacement bursts in pop-in events are discussed.

2. Experiments

2.1. Specimen and microscopic observation

Ni-based single crystal superalloys were prepared by a cylindrical bar with a diameter of 1.5 cm and a length of 17 cm. Its chemical composition mainly contains Cr, Co, W, Ta and Re elements. The samples with a thickness of 1 mm for nanoindentation tests and electron microscopy observations were sliced from a cylinder using a diamond wire saw. Then, they were electrochemically polished through a DC power supply with an electrolyte consisting of 40% sulfuric acid and 60% deionized water at room temperature (see Fig. S1 in supplementary materials). The surface quality of electrochemically polished specimens was carefully examined to ensure that there was no significant mechanical damage or a work hardening layer [26,27].

Before nanoindentation, microstructures of a specimen were characterized by transmission electron microscope (TEM, JEOL JEM-2100F) and scanning electron microscope (SEM, ZEISS Supra-55). Foil for TEM observation was thinned and polished to a thickness of 50 μm, and then punched to a disc of 3 mm in diameter and further perforated by twin-jet electro-polishing with solution of 5 vol% perchloric acid and 95 vol% alcohol at a temperature of −45 °C and a voltage of 65 V [28,29]. Based on the TEM image, Ni-based single crystal superalloys exhibit a mosaic structure that consists of a precipitated phase Ni$_3$Al with an average size of ~500 nm in edge length and a matrix phase Ni with an average

thickness of ~70 nm (see Fig. 1(a)). Fig. 1(b) further shows single misfit dislocations of the Ni$_3$Al/Ni interphase interface misfit dislocation network before the application of any indentation. In addition, the ZEISS Supra-55 SEM with electron backscattering diffraction (EBSD) was used to characterize the crystalline orientation. The EBSD images indicate that the surface normal of samples is along the [001] crystalline orientation (Fig. S2). Finally, the surface indentation morphology of a sample was observed by SEM after nanoindentation.

2.2. Nanoindentation tests

Nanoindentation was carried out with an Agilent Nano Indenter G200 testing system to evaluate hardness and indentation behaviors of Ni-based single crystal superalloys. Indentation tests were made by a diamond Berkovich indenter with a nominal radius of 230 nm, whose area function was determined through calibration with a fused silica standard specimen. All indentations were performed under a constant loading rate of 0.05 s^{-1}. During indentation, continuous stiffness measurement [30,31] was adopted with a harmonic frequency of 75 Hz and a root mean squared displacement amplitude of 2 nm. A prescribed target depth ranging from 50 to 400 nm was set before unloading. >30 indentations were measured at each target depth in arrays with a spacing of 10 μm to avoid interference between adjacent indentations. After that, SEM observations were adopted to pick out indentations located at the Ni$_3$Al precipitate with the maximum indentation depth of 50 nm in order to compare with MD simulations. Further, data with the maximum indentation depth exceeding 50 nm were verified by the indentation depth effect on hardness of the entire composite structure. The indentation force- and hardness-depth curves were extracted to analyze mechanical properties and indentation behaviors [32].

3. Numerical simulations

3.1. Molecular dynamic models

Ni-based single crystal superalloys consist of the pure face-centered cubic Ni matrix and L1$_2$ Ni$_3$Al precipitates, which cause mismatch of a Ni$_3$Al/Ni interfacial lattice [33]. As is known, lattice misfit corresponds to deformation of an invariant lattice. The mismatch δ is defined as the normalized difference of a lattice parameter between Ni and Ni$_3$Al phases, that is

$$\delta = 2\frac{a_{\gamma'} - a_{\gamma}}{a_{\gamma'} + a_{\gamma}} \tag{1}$$

where a_{γ} is 3.52 Å for Ni and $a_{\gamma'}$ is 3.573 Å for Ni$_3$Al [34]. For the Ni$_3$Al/Ni system, δ is 1.5%. As the mismatch exceeds the limit of elasticity, Ni$_3$Al/Ni interfacial misfit dislocation network can be formed on interphase interface to reduce distorted energy of the system. Considering the concept of a coincident site lattice on a misfit interphase interface, such a relationship can be written as

$$na_{\gamma'} = (n+1)a_{\gamma} \tag{2}$$

where n is the n-fold of lattice parameter, which is represented as

$$n = \frac{a_{\gamma}}{a_{\gamma'} - a_{\gamma}}. \tag{3}$$

As to the coincident site lattice on a misfit interphase interface, there are at least 66 Ni$_3$Al and 67 Ni lattices to relax stress induced by the difference of lattice parameters. As shown in Fig. 2(a), the Ni$_3$Al/Ni mosaic structure contains a Ni$_3$Al precipitated cube with a size of 23.6 × 23.6 × 23.6 nm^3 surrounded laterally by Ni matrix with a thickness of 1.4 nm. The thickness of bottom Ni matrix is set to be 2.8 nm (see Fig. 2 (a)). Therefore, the Ni$_3$Al/Ni mosaic substrate is created in a cubic shape with a size of 26.4 × 26.4 × 26.4 nm^3 along the [010], [001] and [100] directions, containing ~1,634,000 atoms. The bottom region with a
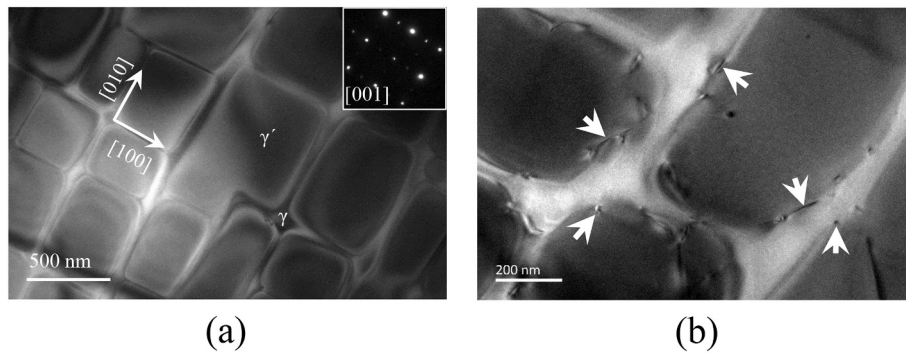
Fig. 1. (a) The microstructure of Ni-based single crystal superalloys obtained by TEM. γ and γ' represent the Ni matrix and Ni₃Al precipitated phases, respectively. Inset at the upper right corner is the selected area electron diffraction pattern. (b) The TEM image of the interfacial misfit dislocation network with arrow heads marking the dislocations.
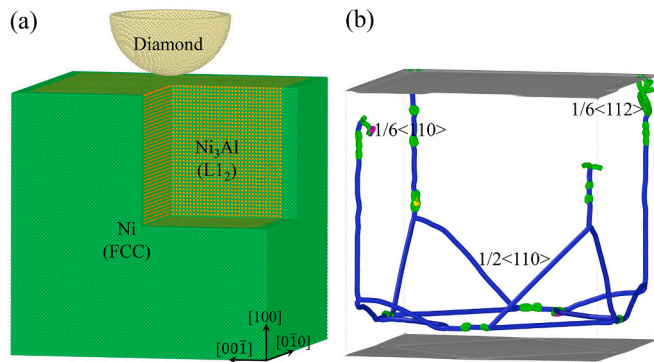
Fig. 2. (a) The MD nanoindentation simulation model for a Ni₃Al/Ni mosaic structure, (b) the Ni₃Al/Ni interfacial misfit dislocation network after relaxation by dislocation analysis with green, purple and blue lines indicating 1/6⟨112⟩ Shockley, 1/6⟨110⟩ stair-rod and 1/2⟨110⟩ perfect dislocations, respectively, and FCC structures are removed for clarity.

thickness of 1.0 nm is frozen. During indentation, free boundary conditions are introduced in lateral directions, allowing dislocations to annihilate at free surface. A hemisphere shell diamond indenter is used with a diameter of 12 nm (~34,000 atoms) and the indentation is along the [001] crystalline orientation. The indenter shape chosen in simulations is based on the fact that, when pop-in events occur below the indentation depth of tens of nm in experiments, the contact area is spherical between an indenter and a sample [35,36]. Thus, the conditions in MD simulations are comparable with that of experiments so that we can focus on the mechanism of pop-in events without noise from the indenter shape and crystalline orientation.

Because of the lattice misfit between Ni and Ni₃Al, an interfacial misfit dislocation network is formed on the Ni₃Al/Ni interphase interface to reduce the distorted energy and accommodate the misfit strain [37]. Here it is worth noting that the interfacial misfit dislocation network was experimentally observed [38,39] and its role in creep rate was analyzed [40]. It is seen from Fig. 2(b) that, due to the influence of top free surface, the Ni₃Al/Ni interfacial misfit dislocation network structure differs from an ideal structure [22,23,37], with parts of 1/2⟨110⟩ perfect dislocations near the top free surface decomposing to several 1/6⟨112⟩ Shockley dislocations.

3.2. Potential function and numerical methods

Atomistic simulations were performed by using the Largescale Atomic/Molecular Massively Parallel Simulator [41]. A potential function based on the embedded-atom method for the Ni-Al system was taken to describe interatomic interactions in Ni₃Al and Ni [42,43]. In

such a function, the total energy, *U*, of a system is written as

$$U = \sum_{\substack{i,j \\ i \neq j}} V_{EAM}(r_{ij}) + \sum_i F(\overline{\rho_i}) \tag{4}$$

where $V_{EAM}(r_{ij})$, the pair potential, is a function of the distance r_{ij} between atoms *i* and *j*, *F* is the embedding energy of atom *i*, and $\overline{\rho_i}$ is the electron density, which can be calculated by

$$\overline{\rho_i} = \sum_{i \neq j} g_j(r_{ij}) \tag{5}$$

where $g_j(r_{ij})$ is the electron density of atom *j*. The force between the diamond indenter and Ni₃Al/Ni mosaic substrate is defined with a two-body Lennard-Jones potential function [44], that is,

$$E = 4 \sum_{\substack{i,j \\ i \neq j}} \varepsilon_{ij} \left[\left(\frac{\sigma_{ij}}{r_{ij}}\right)^{12} - \left(\frac{\sigma_{ij}}{r_{ij}}\right)^6 \right] \tag{6}$$

where ε_{ij} and σ_{ij} are the cohesive energy and the equilibrium distance. Their values are 2.31×10^{-4} eV, 0.2852 nm for C-Ni interactions [45], and 3.15×10^{-4} eV, 0.2976 nm for C-Al interactions [46], respectively. The cutoff distance is 0.8 nm. Here C denotes carbon, the chemical element consisting of the diamond indenter. It is shown that the embedded-atom method for the Ni-Al system and the two-body Lennard-Jones potential function can well describe the nanoindentation properties of Ni-based single crystal superalloys [19,20,23].

Nanoindentation simulations were carried out by integrating Newton's equations of motion for all atoms with a time step of 1 fs. At the start of simulations, initial configurations were energetically minimized by relaxing all samples for 50 ps at 1 K to avoid the temperature effect. The indentation speed and step increment were 10 m s⁻¹ and 2.0×10^{-2} nm, respectively. The maximum indentation depth was 4 nm. Deformation and the dislocation evolution within Ni₃Al/Ni mosaic substrate can be recognized via the common neighbor and dislocation analysis and then, they were visualized with software OVITO [47].

4. Results

4.1. Pop-in events in nanoindentation

Fig. 3 shows typical force- and hardness-depth curves of Ni-based single crystal superalloys from indentation normal to the sample (001) crystal surface with the maximum indentation depth of 50 nm. As indentation depth is <13 nm, indentation force increases until it arrives at a peak value, declaring the elastic deformation and following the Hertzian contact theory [48]. Then, a sudden displacement burst occurs, corresponding to a hardness drop, namely a pop-in event
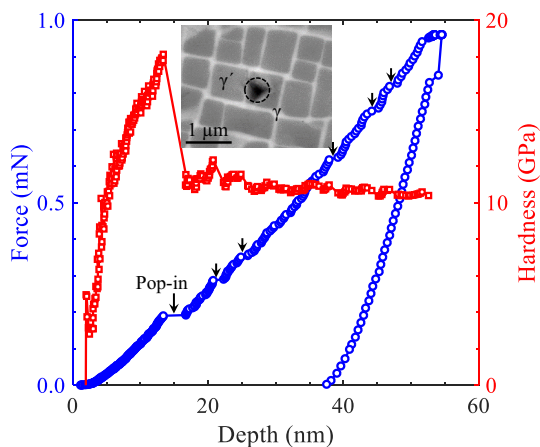
Fig. 3. Typical indentation force- and hardness-depth curves of Ni-based single crystal superalloys with pop-in events marked by black arrows. Inset is the SEM morphology of indentation.

[10,12,15,49–51]. Subsequently, with the increase of indentation depth, force increases and similar pop-in events appear. Finally, hardness gradually decreases to 10.5 GPa at the maximum indentation depth. Here, it is worth noting that all pop-in events can be classified into two categories by magnitudes of their displacement bursts: the first pop-in and the subsequent pop-in events. The first pop-in event produces a larger magnitude of displacement burst, which is two times of that of subsequent pop-in events (see Table 1) by counting 13 sets of data with the maximum indentation depth of 50 nm. Based on the morphology, indentation is located in the Ni_3Al precipitated phase (see inset, the SEM morphology, in Fig. 3).

As the maximum indentation depth increases beyond 50 nm, pop-in events were also observed (see Figs. S3 and S4 in supplementary materials). Since the indentation area contains both Ni_3Al precipitates and Ni matrix separated by Ni_3Al/Ni interfaces (see Fig. S4), it implies that Ni_3Al/Ni interfaces do not affect the occurrence of pop-in events. When the maximum indentation depth increases to 400 nm, hardness decreases from 9.8 to 7.0 GPa, as shown in Fig. S5(a). These values can be well fitted by the Nix-Gao model [52], which shows that the square of hardness is inversely proportional to the maximum indentation depth (see Fig. S5(b)). This provides evidence for the effectiveness of our nanoindentation experiments.

4.2. Dislocation reaction during pop-in events

To better understand pop-in events, MD indentation simulations were performed with dislocation activities being monitored (see Fig. 4 and Fig. S6). It is seen that, as the increase of indentation depth from 0 (point A in Fig. 4), indentation force- and hardness-depth curves rise with the Ni_3Al/Ni interfacial misfit dislocation network structure remaining stable (see Fig. 5). Further, when indentation depth arrives at 0.7 nm (point B in Fig. 4), a $1/6 < 112>$ Shockley dislocation (Fig. 5(b)) nucleates with a layer of tilted stacking fault behind it (hereafter the $1/6 < 112>$ Shockley dislocation is referred to as the $1/6 < 112>$ dislocation and similar terms are adopted for other dislocations). With the indentation depth reaching 0.92 nm (point C in Fig. 4), the indentation force-depth curve arrives to its peak, marking initiation of the first pop-in event. The configurational analysis shows that a few half-prismatic dislocation loops (half-PDLs) adhere under the upper surface of the

Table 1
The corresponding displacement bursts of pop-in events from experimental data.

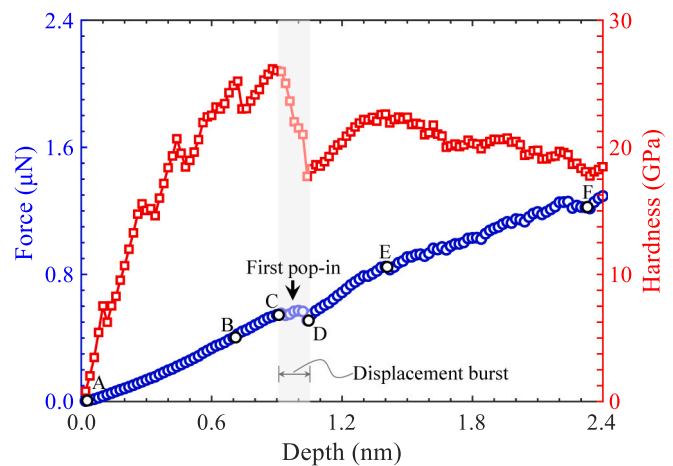| Pop-in event	1-st	2-nd	3-rd	4-th	5-th	6-th
Displacement burst (nm)	3.64	1.48	1.18	1.33	1.28	1.17

Fig. 4. The indentation force- and hardness-depth relationships of Ni_3Al/Ni mosaic structure obtained by an MD nanoindentation simulation, where the black arrow indicates the first pop-in event and the shadow region represents its displacement burst.

Ni_3Al/Ni mosaic substrate (see Fig. 5(c)). The displacement burst resulting from the first pop-in event ranges from 0.92 to 1.04 nm of indentation depth. During the first pop-in event, indentation force is almost unchanged at 0.55 μN, whereas the corresponding hardness exhibits a sudden drop from 27.2 to 17.5 GPa. It is also shown that, at an indentation depth of 1.04 nm (point D in Fig. 4), several stacking fault tetrahedrons (SFTs) appear due to dislocation reactions (see Fig. 5(d)). Specifically, several half-PDLs nucleate at the beginning of the first pop-in event (see Fig. 6(a). Then, one $1/6 < 112>$ dislocation from an extended dislocation in a half-PDL merges with the other $1/6 < 112>$ dislocation from another half-PDL. The reaction can be written as $1/6 [211] + 1/6[\bar{2}11] \rightarrow 1/3[011]$. The newly formed $1/3[011]$ acts as a boundary of an SFT (Fig. 6(b)). At the same time, another dislocation reaction with the form of $1/6[12\bar{1}] + 1/6[1\bar{2}1] \rightarrow 1/3[10\bar{1}]$ happens (Fig. 6(c)). These dislocation reactions can be detected from the change of dislocation lengths. It is seen from Fig. 7 that, as indentation depth increases from 0.92 to 0.98 nm, the length of $1/6 < 112>$ dislocation increases, while that of $1/3 < 110>$ dislocation remains unchanged. However, within the subsequent indentation depth ranging from 0.98 to 1.04 nm, lengths of the $1/6 < 112>$ and $1/3 < 110>$ dislocations undergo opposite variations due to $1/6 < 112>$ dislocations merging into $1/3 < 110>$ dislocations. Such dislocation reactions result in formation of SFTs with the $1/3 < 110>$ dislocations acting as their boundaries (see Fig. 6(d) and Video S1). The completion of constructing SFTs precisely corresponds to the end of the first pop-in event.

As indentation depth further increases to 1.4 nm (point E in Fig. 4), the hardness-depth curve reaches its local peak. The SFTs are still partially stable, although parts of them have decomposed to extended dislocations and propagated downward into Ni_3Al precipitate (see Fig. 5(e)). However, with the increase of indentation depth, SFTs decompose to half-PDLs. These half-PDLs further extend into the interior of Ni_3Al precipitate (see Fig. 5(f)). Here it is worth noting that, below an indentation depth of 2.3 nm (point F in Fig. 4), the interfacial misfit dislocation network does not change. However, with the continuous increase of indentation depth, the interfacial misfit dislocation network decomposes and interacts with half-PDLs, resulting in an indentation force oscillating around 1.4 μN (see Figs. S6 and S7 in supplementary materials). In addition, hardness (after the first pop-in) initially increases and then continuously decreases with indentation depth in the MD simulation (see Fig. 4 with the indentation depth from 1.04 to 1.4 nm). Such a tendency was also observed in experimental results (see Fig. 3 with the indentation depth from 16 to 21 nm). This consistency is attributed to the lateral free boundary conditions in our atomistic
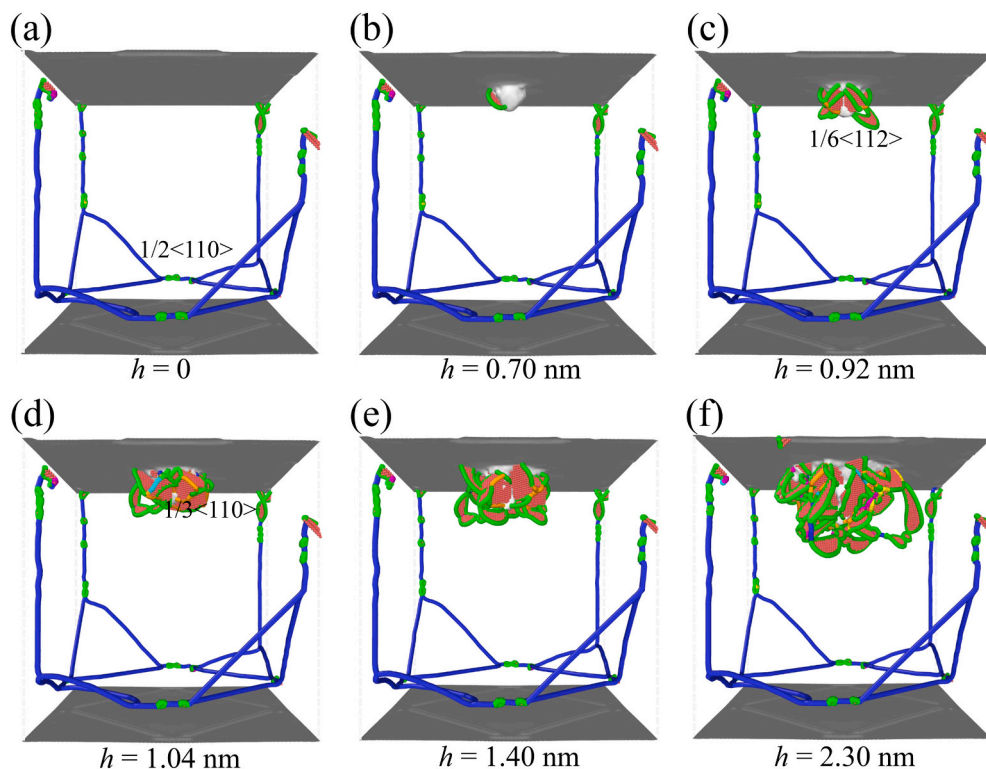
Fig. 5. Dislocations evolve in Ni₃Al/Ni mosaic substrate at various indentation depths of (a) 0, (b) 0.70, (c) 0.92, (d) 1.04, (e) 1.40 and (f) 2.30 nm, corresponding to points A–F in Fig. 4. Structures of dislocations visualized by dislocation analysis with green, purple, orange, yellow and blue lines indicating 1/6<112> Shockley, 1/6<110> stair-rod, 1/3<110>, 1/3<100> Hirth, and 1/2<110> perfect dislocations, respectively. Red atoms representing stacking faults and FCC structures are removed for clarity.
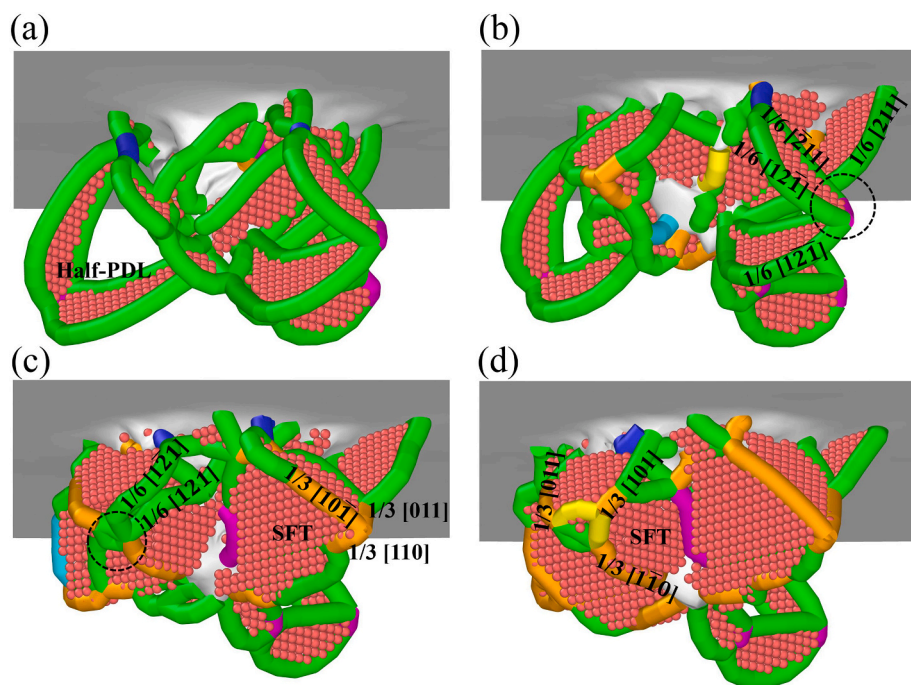
Fig. 6. The process of 1/6<112> + 1/6<112> → 1/3<110> dislocation reactions during the first pop-in event at various indentation depths of (a) 0.96, (b) 1.00, (c)1.02 and (d)1.04 nm. Black dash circles represent spots at which dislocation reactions happen. Microstructural evolution is analyzed by the dislocation analysis, with stacking fault atoms being colored in red. 1/6<112> Shockley, 1/2<110> perfect, 1/6<110> stair-rod, 1/3<110> and 1/3<100> Hirth dislocations are shown with green, blue, purple, orange, and yellow lines.

simulation model, which allow annihilation of dislocations at free surfaces. On the contrary, the lateral periodic boundary conditions miss this consistency [53,54].

The decomposing process of SFTs initiates from decomposition of their lower boundaries (1/3 < 110> dislocations) (see Fig. 8(a), which shows two SFTs). The decomposing reaction of a 1/3 < 110> dislocation undergoes exactly the reverse reaction as it forms, i.e., 1/3 < 110> → 1/6 < 112> + 1/6 < 112>. The newly produced 1/6 < 112> dislocations

extend downward into Ni₃Al precipitate (see Fig. 8(b)). With the further increase of indentation depth, the entire left SFT has completely decomposed to 1/6 < 112> extended dislocations (Fig. 8(c)). Finally, all of the SFTs formed during the first pop-in event decompose to 1/6 < 112> extended dislocations and half-PDLs (see Fig. 8(d) and Video S2).

Similarly, subsequent pop-in events also precisely relate to formation of new SFTs after decomposition of old ones. Although the space under an indenter in Ni₃Al precipitate is full of disorganized 1/6 < 112>
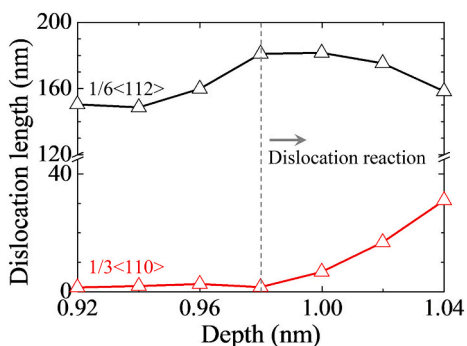
Fig. 7. Lengths of 1/6<112> and 1/3<110> dislocations change with the indentation depth during the first pop-in event.

extended dislocations and half-PDLs, their frequent merging and decomposing reactions lead to generation of a new SFT by coincidence (see Fig. 9 and Video S3). In contrast to the first pop-in event, formation of a new SFT always confronts the same spatial condition during subsequent pop-in events. This brings almost the same magnitude of subsequent displacement bursts.

5. Discussion

As seen in Fig. 10(a), displacement bursts of subsequent pop-in events are about half of the magnitude of the first pop-in event. To show the correlation of pop-in events between experiments and MD simulations, displacement bursts are respectively normalized by their own values, corresponding to their first pop-in events. This consistency between the experimental data and MD simulations partially verifies the dislocation reactions that dominated the magnitude of displacement bursts of pop-in events. It is expected that the dislocation reactions can be experimentally observed after establishment of an in-situ nano-indentation system with an accurate temporal and spatial resolution in
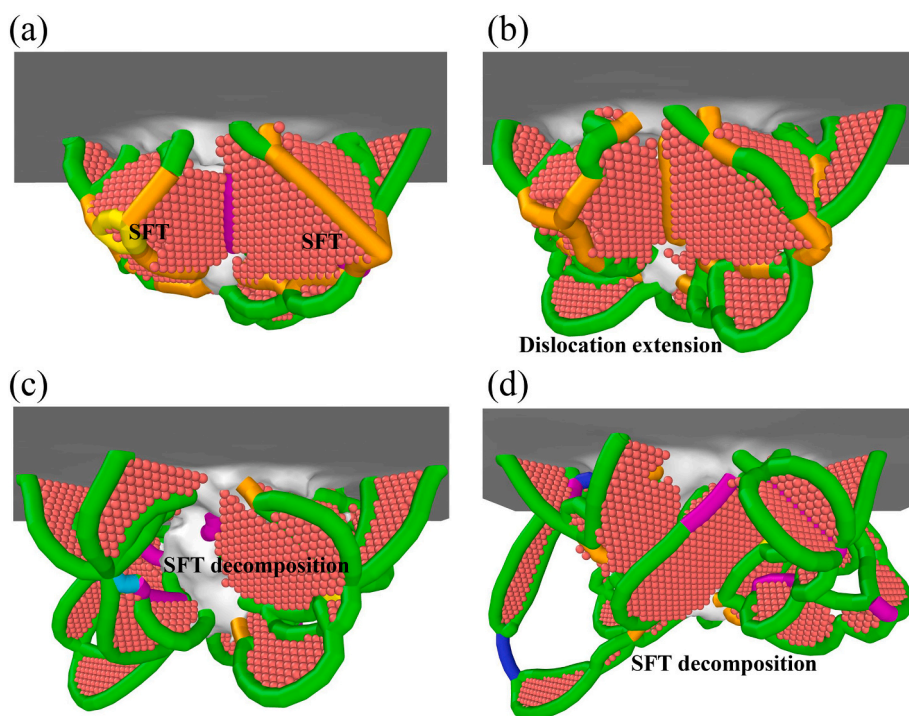

Fig. 8. The decomposing process of SFTs following the first pop-in event at various indentation depths of (a) 1.24, (b)1.44, (c)1.58 and (d)1.74 nm. Microstructural evolution is analyzed by the dislocation analysis, with stacking fault atoms being colored in red. 1/6<112> Shockley, 1/2<110> perfect, 1/6<110> stair-rod, 1/3<110> and 1/3<100> Hirth dislocations are shown with green, blue, purple, orange, and yellow lines.
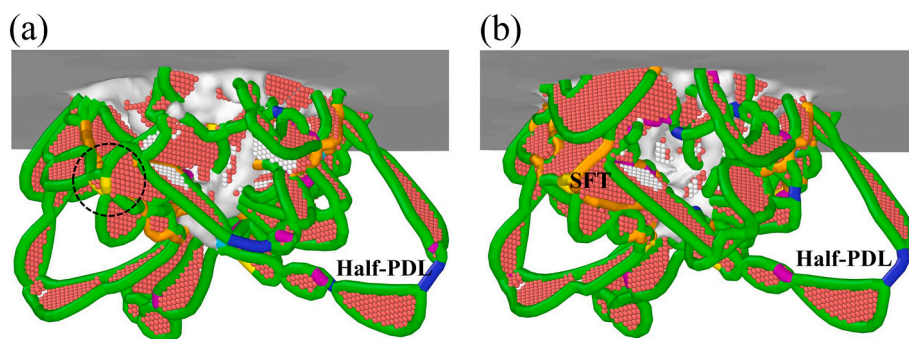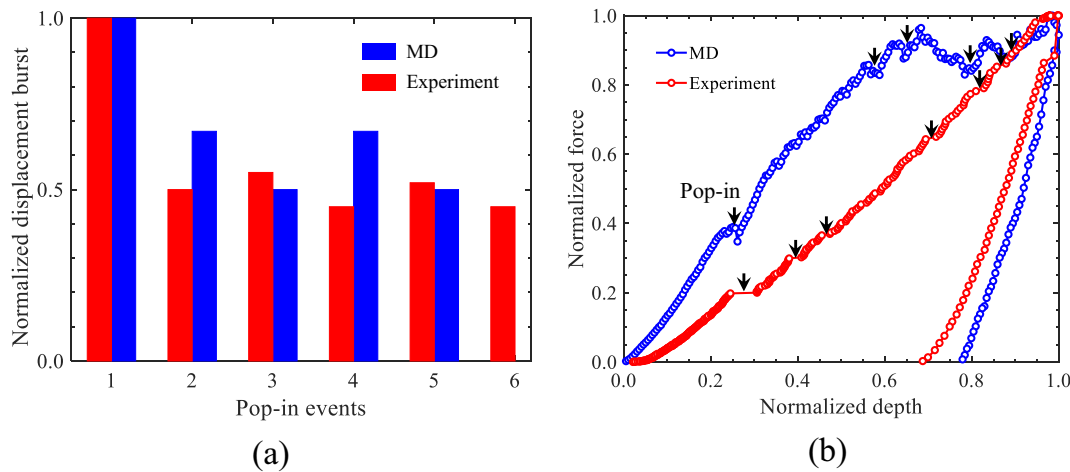

Fig. 9. The generation of a new SFT during the second pop-in event at indentation depths of (a) 2.22 and (b) 2.26 nm. The white atoms represent those involved in the first pop-in event, and a black dash circle marks the spot where dislocation reactions happen, and FCC structures are removed for clarity.

Fig. 10. (a) The normalized magnitudes of displacement bursts in pop-in events (five in MD simulation and six in experiment, respectively) and (b) the normalized force-depth curves, where arrow heads mark the positions of pop-in events.

the future. Fig. 10(b) further shows that the relative position of pop-in events does not coincide between the MD simulation and experiment. This is attributed to pop-in events corresponding to the occasional construction events of SFTs. Therefore, various numbers of pop-in events at flexible positions of a force-depth curve were exhibited in samples [54]. Based on MD simulations, pop-in events are closely related to dislocation reactions that result in SFTs, which are common microstructures in close-packed materials [55,56].

To find out the underlying mechanism of dislocation reactions dominated pop-in events, an energy conversion model was constructed by analyzing the energy conversion between external work and strain energy stored in dislocations and stacking faults [57]. Given that there are no dislocation reactions during a pop-in event, the strain energy stored in dislocation lines is derived by using the model. Then, the energy due to dislocation reactions is taken out and the remnant strain energy can be checked out by external work. Specifically, the strain energy (ξ_d) stored in a dislocation line or curve with a length L can be expressed as

$$\xi_d = \alpha G b^2 L \qquad (7)$$

where α is a coefficient related to the geometry of a dislocation, with $\alpha \approx 1$ for a straight dislocation line and $\alpha \approx 1/2$ for a bent dislocation curve. The latter was adopted because almost all dislocations participating reactions are bent. $G = 77.8$ GPa is the shear modulus of Ni$_3$Al [58], and b is the magnitude of a Burgers vector. For the $1/6 < 112> + 1/6 < 112> \to 1/3 < 110>$ dislocation reaction, two $1/6 < 112>$ dislocations merge to one $1/3 < 110>$ dislocation in length (hereafter, the $1/6 < 112> + 1/6 < 112> \to 1/3 < 110>$ dislocation reaction is referred to as the $1/6 < 112> \to 1/3 < 110>$ reaction for simplicity and similar statements are adopted for other kinds of dislocation reactions). Fig. 7 shows that the length of $1/3 < 110>$ dislocation increases by 29.5 nm during the first pop-in event. Therefore, the length of $1/6 < 112>$ dislocation merged to $1/3 < 110>$ dislocation is $29.5 \times 2 = 59.0$ nm. It can be seen from Fig. 7, the length of $1/6 < 112>$ dislocation increases by 30.6 nm in the indentation depth range of 0.92 to 0.98 nm. Given that the $1/6 < 112> \to 1/3 < 110>$ reaction does not happen, the length of $1/6 < 112>$ dislocation should increase by $59.0 + 30.6 = 89.6$ nm within the indentation depth range of 0.92 to 1.04 nm, corresponding to the first pop-in event. This implies that the strain energy stored in $1/6 < 112>$ dislocation increases by $\alpha G b^2 \Delta L = \alpha G a_{\gamma'}^2 (1/6) \times 89.6 = 7.4 \times 10^{-17}$ J, where $a_{\gamma'} = 0.3573$ nm is the lattice parameter of Ni$_3$Al. In addition, the strain energy stored in stacking faults (ξ_{SF}) varies by

$$\Delta \xi_{SF} = \zeta \Delta A_{SF} \qquad (8)$$

where $\zeta = 125$ mJ m^{-2} is the stacking fault energy of Ni$_3$Al [59], and A_{SF} is the area of stacking faults. Since A_{SF} grows by 5.8×10^{-17} m^2, the strain energy stored in stacking faults rises by 7.3×10^{-18} J. Adding them together, the strain energy stored in dislocations and stacking faults goes up by 8.1×10^{-17} J due to growth of $1/6 < 112>$ dislocation and stacking faults if the $1/6 < 112> \to 1/3 < 110>$ reaction does not happen within the depth range of the first pop-in event. Since the growth of $1/6 < 112>$ dislocation and stacking faults converts external work imposed by the indenter to strain energy, it leads to reduction of loading force. This can be observed from indentation force-depth curves with generation of simple dislocation structures such as edge dislocation dipoles and PDL pairs in Ni$_3$Al [22,23].

Without an external force, a spontaneous dislocation reaction complies with two conditions. The first condition demands that Burgers vectors are conserved with a reaction, and the second one requires that the strain energy stored in dislocations reduces after the reaction. With an external force, however, the second condition can be broken and the strain energy stored in dislocations may rise due to dislocation reactions. Based on Eq. (7), the released strain energy due to the $1/6 < 112> \to 1/3 < 110>$ reaction is $\alpha G a^2 (6/36 + 6/36 - 2/9) \times 29.5 = 1.6 \times 10^{-17}$ J. Then, the strain energy stored in dislocations and stacking faults is derived as $(8.1 - 1.6) \times 10^{-17} = 6.5 \times 10^{-17}$ J during the first pop-in event. This is well consistent with the external work (W) of 6.6×10^{-17} J calculated by.

$$W = \bar{f} S \qquad (9)$$

where $\bar{f} = 0.55$ μN and $S = 0.12$ nm are the average force and the magnitude of a displacement burst during the first pop-in event. Here the negligible difference results from other kinds of unconsidered dislocations with lengths varying below 3 nm and dissipation energy by dislocation glide.

Similarly, subsequent pop-in events can be analyzed. However, in addition to the main $1/6 < 112> \to 1/3 < 110>$ reaction, dislocation reactions during subsequent pop-in events are quite complicated, involving such as the $1/6 < 112> + 1/6 < 112> \to 1/3 \langle 100 \rangle$ merging and the $1/2 < 110> \to 1/6 < 112> + 1/6 < 112> + 1/6 < 110>$ decomposing reactions. As shown in Fig. 11, the length of diverse dislocations drastically varies during the second pop-in event, denoting occurrence of frequent merging and decomposing reactions. Although analysis on the energy conversion is difficult through the entire second pop-in event, it is still implemented within a depth range with few dislocation reactions. Here, the indentation depth range is chosen from 2.20 to 2.22 nm (see Fig. 11). Owing to growth of $1/6 < 112>$ dislocations, strain energy increases by 2.7×10^{-17} J. In addition, the strain
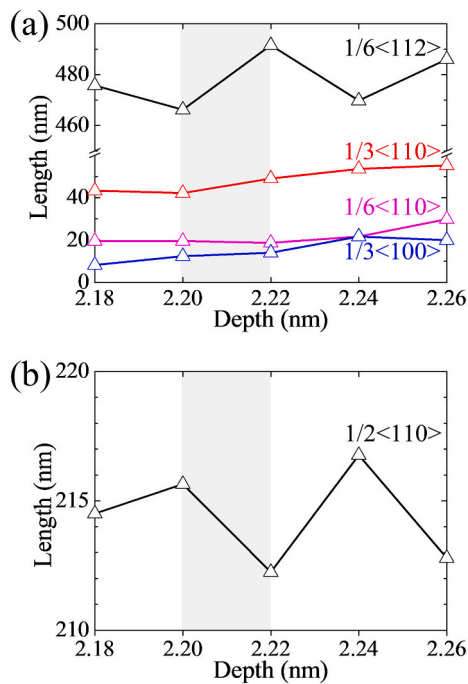
Fig. 11. Lengths of (a) 1/6<112>, 1/6<110>, 1/3<110> and 1/3<100> and (b) 1/2<110> dislocations vary with indentation depths during the second pop-in event, with shadow regions selected for analysis of energy conversion between external work and strain energy.

Table 2

Dislocation reactions and the energy conversion between external work and strain energy stored in dislocations during pop-in events. Values in brackets are selected for analysis of energy conversion during subsequent pop-in events.

Pop-in	Depth range (nm)	Average force (μN)	Dislocation reactions	Strain energy (× 10^{-17} J)	External work (× 10^{-17} J)
1-st	0.92–1.04	0.55	$1/6 < 112> + 1/6 < 112> \rightarrow 1/3 < 110>$	6.5	6.6
2-nd	2.18–2.26 [2.20–2.22]	1.15	$1/6 < 112> + 1/6 < 112> \rightarrow 1/3 < 110>$ $1/2 < 110> \rightarrow 1/6 < 112> + 1/6 < 112> + 1/6 < 110>$	2.2	2.3
3-rd	2.40–2.46 [2.42–2.44]	1.32	$1/6 < 112> + 1/6 < 112> \rightarrow 1/3 < 110>$ $1/6 < 112> + 1/6 < 112> \rightarrow 1/3 < 100>$ $1/6 < 112> + 1/6 < 112> \rightarrow 1/6 < 110>$	1.6	2.6
4-th	3.18–3.26 [3.20–3.22]	1.25	$1/6 < 112> + 1/6 < 112> \rightarrow 1/3 < 110>$ $1/3 < 100> \rightarrow 1/6 < 110> + 1/6 < 110>$ $1/6 < 112> + 1/6 < 112> \rightarrow 1/3 < 110>$	1.9	2.5
5-th	3.52–3.58 [3.54–3.56]	1.29	$1/6 < 112> + 1/6 < 112> \rightarrow 1/3 < 100>$ $1/6 < 112> + 1/6 < 112> \rightarrow 1/3 < 110>$ $1/2 < 110> \rightarrow 1/6 < 112> + 1/6 < 112> + 1/6 < 110>$	2.2	2.6

energy stored in stacking faults raises by 1.2×10^{-18} J. Then, the released strain energies due to the $1/6 < 112> \rightarrow 1/3 < 110>$ and the $1/2 < 110> \rightarrow 1/6 < 112> + 1/6 < 112> + 1/6 < 110>$ reactions are 0.4×10^{-17} J and 0.2×10^{-17} J, respectively. Putting them together, the strain energy stored in dislocations and stacking faults goes up by 2.2×10^{-17} J, which is consistent with the external work of 2.3×10^{-17} J within the indentation depth range of 2.20 to 2.22 nm.

As seen from Table 2 and Fig. S8, energy is absorbed during growth of $1/6 < 112>$ dislocations, representing that the external work is transferred to strain energy stored in dislocations and stacking faults. In contrast, dislocation reactions to form SFTs release strain energy and this implies that the Ni₃Al/Ni mosaic substrate does work to the exterior. The balancing effect between energy absorption and release produces a plateau in the force-depth curve, indicating occurrence of a pop-in event. It is obvious that, during the first pop-in event, only the $1/6 < 112> \rightarrow 1/3 < 110>$ merging reaction happens. There is plenty of space in the Ni₃Al precipitate for growth of $1/6 < 112>$ dislocations. This prolongs the reaction time if dislocations react at a constant rate and thus leads to a bigger magnitude of displacement burst during the first pop-in event. However, subsequent pop-in events appear as new SFTs form through merging and decomposing dislocation reactions in the region full of disorganized $1/6 < 112>$ extended dislocations and half-PDLs. This, therefore, brings almost the same magnitude of displacement bursts during subsequent pop-in events. This also leads to the growing deviation of strain energy stored in dislocations and stacking faults from the external work during subsequent pop-in events as the energy conversion model is adopted.

Shibutani et al. [11] explored the pop-in events and their mechanisms by theoretical analyses. Instead of the energy evolution of dislocation reactions, their focus was on the slip of perfect dislocations and activation of partial dislocations. Here, our energy conversion and MD models are checked out by Ni-based single crystal superalloys in the present work. Since the lattice parameters, such as that in face-centered cubic, body-centered cubic and hexagonal close packed materials, are involved in the models, it is expected that they can be extended and

applied to depict the mechanical properties dominated by dislocation activities (e.g., reaction and annihilation) in other metals or alloys. Factors such as the crystal structure, loading and surface orientation can also affect the magnitude of displacement bursts. However, they are not taken into account because pop-in events originate from dislocation activities in nature. Thus, the energy conversion model and its accuracy depend on dislocation reaction forms (e.g., decomposition and mergence), dislocation types (e.g., $1/6 < 112>$ Shockley and $1/3 < 100>$ Hirth), and the length of dislocation lines.

The discrepancy of hardness between experimental and MD simulation results originates from sample and indenter sizes and loading rates. This precisely reflects the physical mechanism since the mechanical properties such as yield strength and hardness increase with the decrease of sample and indenter sizes and the increase of loading rates [60–62]. Moreover, dislocations in an L1₂ structure tend to propagate in pairs since their minimum Burgers vector is two times of that of a face-centered cubic structure [20]. In addition, given that there is an elastic to plastic transition in Ni₃Al/Ni mosaic substrate, occurring at the initiation of the first pop-in event, the indenter tip can be roughly considered as a spherical shape in both experiments and numerical simulations. Then, the size-independent indentation modulus E^* can be calculated by using the Hertz formula, $E^* = \frac{3P}{4\sqrt{R}\sqrt{h^3}}$, where P and h represent force and indentation depth at the initiation of the first pop-in

event, and R indicates the radius of an indenter. As listed in Table 3, the value of E^* from experimental data accords well with that from MD results, which is consistent with the previous experimental results [63]. Here it is worth noting the influence of the dissimilar loading rate on the indentation hardness discrepancy between the MD and experimental results. Normally, the MD simulation carries out at a loading rate of 4.2×10^8 s^{-1} while it is ~0.05 s^{-1} in experiments. Therefore, the MD simulation with a higher loading rate usually generates a bigger indentation hardness at the initiation of the first pop-in event in contrast to that in experiments. However, the discrepancy of hardness at the elastic regime between experimental data and MD simulations has no influence on dislocation evolution mechanisms at the plastic regime corresponding to pop-in events induced by occasional construction of SFTs.

Moreover, according to studies on the dimensional dependence of hardness and dislocation evolution during nanoindentation processes [64], total and geometrically necessary dislocation densities, as well as hardness, increase with decreasing depths. In the present work, the indentation depth effect of Ni-based single crystal superalloy shows that the square of hardness is inversely proportional to the maximum indentation depth (see Fig. S5(b)). This trend of hardness varying with depth echoes the results of Javaid et al. [64]. Furthermore, we calculated the energy conversion during the evolution (formation or decomposition) of the $1/2 < 110 >$ full dislocation during pop-in events. The result shows that its evolution accounts for <10% of the entire energy conversion. That is, the $1/2 < 110 >$ full dislocation makes a little contribution to mediate pop-in events.

6. Conclusions

In this paper, we have combined nanoindentation experiments with MD simulations to investigate the pop-in events in Ni-based single crystal superalloys, particularly on Ni$_3$Al precipitate. It is shown that there is a serial of pop-in events in indentation force-depth curves. MD simulations revealed that pop-in events result from formation of SFTs due to dislocation reactions. An energy conversion model was built to analyze the energy conversion between the external work and strain energy stored in dislocations. The main conclusions can be summarized as follows:

(1) The pop-in events correspond to a process of continuously constructing SFTs in Ni$_3$Al precipitate. SFTs can decompose to $1/6 < 112 >$ extended dislocations and half-PDLs.
(2) There is only one kind of dislocation reaction during the first pop-in event. As two $1/6 < 112 >$ dislocations meet, they react and merge into a $1/3 < 110 >$ dislocation, which acts as a boundary of an SFT.
(3) The formation of new SFTs during subsequent pop-in events is accompanied by merging and decomposing dislocation reactions at the space full of $1/6 < 112 >$ extended dislocations and half-PDLs. This leads to almost the same magnitude of displacement bursts, which is half of that in the first pop-in event.
(4) The continuous generation of $1/6 < 112 >$ dislocations converts the external work to strain energy stored in dislocations, while dislocation reactions to form SFTs release the strain energy. The balance of energy conversion between external work and strain energy yields a plateau in a force-depth curve, denoting occurrence of a pop-in event.

It is expected that these findings can provide new insights into a deep understanding of the deformation mechanism of pop-in events in Ni-based single crystal superalloys and benefit their wide applications in the aerospace industry.

Supplementary data to this article can be found online at https://doi.org/10.1016/j.matchar.2023.112883.

Table 3
The indentation modulus E^* obtained from the experimental data and MD results by using the Hertz formula. Here P and h denote the force and indentation depth at initiation of the first pop-in event and R represents the radius of an indenter tip.

	P (N)	R (mm)	h (mm)	E^* (GPa)
Experimental data	1.8×10^{-4}	1.0×10^{-4}	1.3×10^{-5}	189.9
MD results	5.5×10^{-7}	6.0×10^{-6}	9.2×10^{-7}	190.8

CRediT authorship contribution statement

Zhiwei Zhang: Conceptualization, Investigation, Methodology, Data curation, Writing – original draft, Writing – review & editing. **Wei Cai:** Formal analysis, Writing – review & editing. **Jun Wang:** Conceptualization, Supervision, Writing – review & editing, Funding acquisition. **Rong Yang:** Funding acquisition, Writing – review & editing. **Pan Xiao:** Funding acquisition, Writing – review & editing. **Fujiu Ke:** Conceptualization. **Chunsheng Lu:** Writing – review & editing.

Declaration of Competing Interest

The authors declare that they have no known competing financial interests or personal relationships that could have appeared to influence the work reported in this paper.

Data availability

The data that support the findings within this paper are available from the corresponding author upon reasonable request.

References

[1] H. Nili, K. Kalantar-zadeh, M. Bhaskaran, S. Sriram, In situ nanoindentation: probing nanoscale multifunctionality, Prog. Mater. Sci. 58 (2013) 1–29.
[2] F. Shuang, K.E. Aifantis, Relating the strength of graphene/metal composites to the graphene orientation and position, Scr. Mater. 181 (2020) 70–75.
[3] F. Shuang, K.E. Aifantis, A first molecular dynamics study for modeling the microstructure and mechanical behavior of Si nanopillars during lithiation, ACS Appl. Mater. Interfaces 13 (2021) 21310–21319.
[4] F. Shuang, Z.H. Dai, K.E. Aifantis, Strengthening in metal/graphene composites: capturing the transition from interface to precipitate hardening, ACS Appl. Mater. Interfaces 12 (2021) 26610–26620.
[5] Y.J. Sato, S.H. Shizato, T. Ohmura, T. Hatano, S. Ogata, Unique universal scaling in nanoindentation pop-ins, Nat. Commun. 11 (2020) 1–9.
[6] X.W. Li, J.S. Liang, T. Shi, D.N. Yang, X.C. Chen, C.W. Zhang, Z.H. Liu, D.Z. Liu, Q.X. Zhang, Tribological behaviors of vacuum hot-pressed ceramic composites with enhanced cyclic oxidation and corrosion resistance, Ceram. Int. 46 (2020) 12911–12920.
[7] X.W. Li, T. Shi, B. Li, X.C. Chen, C.W. Zhang, Z.G. Guo, Q.X. Zhang, Subtractive manufacturing of stable hierarchical micro-nano structures on AA5052 sheet with enhanced water repellence and durable corrosion resistance, Mater. Des. 183 (2019), 108152.
[8] W.J. Lu, J.J. Li, Synergetic deformation mechanism in hierarchical twinned high-entropy alloys, J. Mater. Sci. Technol. 102 (2021) 80–88.

[9] R. Navamathavan, S.J. Park, J.H. Hahn, C.K. Choi, Nanoindentation 'pop-in' phenomenon in epitaxial ZnO thin films on sapphire substrates, Mater. Charact. 59 (2008) 359–364.

[10] Y.Z. Xia, Y.F. Gao, G.M. Pharr, H.B. Bei, Single versus successive pop-in modes in nanoindentation tests of single crystals, J. Mater. Res. 31 (2016) 2065–2075.

[11] Y. Shibutani, T. Tsuru, A. Koyama, Nanoplastic deformation of nanoindentation: crystallographic dependence of displacement bursts, Acta Mater. 55 (2007) 1813–1822.

[12] A. Gouldstone, H.J. Koh, K.Y. Zeng, Discrete and continuous deformation during nanoindentation of thin films, Acta Mater. 48 (2000) 2277–2295.

[13] T.P. Remington, C.J. Ruestes, E.M. Bringa, B. Remington, C.H. Lu, B. Kad, M. A. Meyers, Plastic deformation in nanoindentation of tantalum: a new mechanism for prismatic loop formation, Acta Mater. 78 (2014) 378–393.

[14] S. Vadalakonda, R. Banerjee, A. Puthcode, R. Mirshams, Comparison of incipient plasticity in bcc and fcc metals studied using nanoindentation, Mater. Sci. Eng. A 426 (2006) 208–213.

[15] T.L. Li, Y.F. Gao, H. Bei, E.P. George, Dislocation structure and dynamics govern pop-in modes of nanoindentation on single-crystal metals, J. Mech. Phys. Solids 59 (2011) 1147–1162.

[16] N. Zhou, K.I. Elkhodary, X.X. Huang, S. Tang, Y. Li, Philos. Mag. 100 (2020) 1585–1606.

[17] H. Yang, Z.D. Wang, Y.F. Guo, X.H. Shi, A molecular dynamics investigation of the deformation mechanism and shape memory effect of epoxy shape memory polymers, Sci. China Phys. Mech. 59 (2016), 634601.

[18] X.H. Shi, B. Peng, N.M. Pugno, H.J. Gao, Stretch-induced softening of bending rigidity in graphene, Appl. Phys. Lett. 100 (2012), 191913.

[19] Z.W. Zhang, Q. Fu, J. Wang, P. Xiao, F.J. Ke, C. Lu, Hardening Ni$_3$Al via complex stacking faults and twinning boundary, Comput. Mater. Sci. 188 (2021) 110201.

[20] Z.W. Zhang, Q. Fu, J. Wang, R. Yang, P. Xiao, F.J. Ke, C. Lu, Interactions between butterfly-like prismatic dislocation loop pairs and planar defects in Ni$_3$Al, Phys. Chem. Chem. Phys. 23 (2021) 10377–10383.

[21] Z.W. Zhang, Q. Fu, J. Wang, R. Yang, P. Xiao, F.J. Ke, C. Lu, Simultaneously achieving strength and ductility in Ni3Al nanowires with superlattice intrinsic stacking faults, Int. J. Mech. Sci. 215 (2022), 106953.

[22] Z.W. Zhang, Q. Fu, J. Wang, R. Yang, P. Xiao, F.J. Ke, C. Lu, Atomistic modeling for the extremely low and high temperature-dependent yield strength in a Ni-based single crystal superalloy, Mater. Today Commun. 27 (2021), 102451.

[23] Z.W. Zhang, Q. Fu, J. Wang, R. Yang, P. Xiao, F.J. Ke, C. Lu, Interaction between the edge dislocation dipole pair and interfacial misfit dislocation network in Ni-based single crystal superalloys, Int. J. Solids Struct. 228 (2021), 111128.

[24] A.R. Khoei, M. Youzi, G.T. Eshlaghi, Mechanical properties and interfacial misfit network evolution: a study towards the creep behavior of Ni-based single crystal superalloys Mech, Mater. 171 (2022), 104368.

[25] Z.H. Dai, N.S. Lu, K.M. Liechti, R. Huang, Mechanics at the interfaces of 2D materials: challenges and opportunities, Curr. Opin. Solid State Mater. Sci. 24 (2020), 100837.

[26] F.S. Yuan, F.Z. Han, Y.D. Zhang, A.L. Muhammad, W.B. Guo, J. Ren, C.Z. Liu, H. F. Gu, G.P. Li, G.H. Yuan, Intermediate state of hexagonal close-packed structure to face-centered cubic structure transformation: direct evidence for basal-type face-centered cubic phase via partial dislocation in zirconium, J. Mater. Sci. Technol. 98 (2022) 44–50.

[27] Z.H. Wu, L.C. Zhang, Mechanical properties and deformation mechanisms of surface-modified 6H-silicon carbide, J. Mater. Sci. Technol. 90 (2021) 58–68.

[28] H.B. Long, S.R. Bakhtari, Y.N. Liu, S.C. Mao, H. Wei, Y.H. Chen, A. Li, D.L. Kong, L. Yan, L.Y. Yang, Z. Zhang, X.D. Han, A comparative study of rafting mechanisms of Ni-based single crystal superalloys, Mater. Des. 196 (2020), 109097.

[29] W.L. Ren, C.L. Niu, B. Ding, Y.B. Zhong, J.B. Yu, Z.M. Ren, W.Q. Liu, L.P. Ren, P. K. Liaw, Improvement in creep life of a nickel-based single-crystal superalloy via composition homogeneity on the multiscales by magnetic-field-assisted directional solidification, Sci. Rep. 8 (2018) 1452.

[30] X.D. Li, B. Bhushan, A review of nanoindentation continuous stiffness measurement technique and its applications, Mater. Charact. 48 (2002) 11–36.

[31] Y.J. Hong, C.S. Zhou, Y.Y. Zheng, L. Zhang, J.Y. Zheng, B. An, X.Y. Chen, X. H. Wang, Hydrogen effect on the deformation evolution process in situ detected by nanoindentation continuous stiffness measurement, Mater. Charact. 127 (2017) 35–40.

[32] Y. Zhou, A. Fillon, D. Laillé, T. Gloriant, Probing grain size effect in the superelastic Ti-20Zr-3Mo-3Sn alloy using spherical nanoindentation, Mater. Charact. 184 (2022), 111691.

[33] M. Seyring, M. Rettenmayr, Impact of crystallography at Ni/NiAl interfaces on the nucleation of Ni$_3$Al, Acta Mater. 208 (2021), 116713.

[34] A.F. Voter, S.P. Chen, Accurate interatomic potentials for Ni, Al and Ni$_3$Al, MRS Proc. 82 (1986) 175.

[35] X.Y. Tang, X.H. Shi, Y. Gan, X. Yi, Nanomechanical characterization of pressurized elastic fluid nanovesicles using indentation analysis, Ext. Mech. Lett. 34 (2020), 100613.

[36] H.T. Luu, S. Raumel, F. Dencker, M. Wurz, N. Merkert, Nanoindentation in alumina coated Al: molecular dynamics simulations and experiments, Surf. Coat. Technol. 437 (2022), 128342.

[37] S.G. Tian, H.H. Zhou, J.H. Zhang, H.C. Yang, Y.B. Xu, Z.Q. Hu, Formation and role of dislocation networks during high temperature creep of a single crystal nickel–base superalloy, Mater. Sci. Eng. A 279 (2000) 160–165.

[38] S.Y. Ma, X.Z. Lv, J.X. Zhang, Y.J. Zhang, P. Li, H.X. Jin, W.Y. Zhang, X.Q. Li, S. C. Mao, Core structure and strengthening mechanism of the misfit dislocation in nickel-based superalloys during high-temperature and low-stress creep, J. Alloys Compd. 743 (2018) 372–376.

[39] Y. Ru, S.S. Li, J. Zhou, Y.L. Pei, H. Wang, S.K. Gong, H.B. Xu, Excellent mechanical properties of CoNiCr-based MP159 multicomponent alloys at ambient and cryogenic temperatures, Sci. Rep. 6 (2016) 29941.

[40] Y.W. Li, L. Wang, Y.F. He, W. Zhang, L.H. Lou, J. Zhang, Role of interfacial dislocation networks during secondary creep at elevated temperatures in a single crystal Ni-based superalloy, Scr. Mater. 217 (2022), 114769.

[41] S. Plimpton, Fast parallel algorithms for short-range molecular dynamics, J. Comput. Phys. 117 (1995) 1–19.

[42] Y. Mishin, Atomistic modeling of the γ and γ'-phases of the Ni–Al system, Acta Mater. 52 (2004) 1451–1467.

[43] J.H. Hao, X.B. Jing, B. Liu, Y. Wang, Z.Q. Wang, W.Z. He, W.J. Zhao, L. Feng, Molecular dynamics simulations on shock induced plasticity and stacking fault of coherent {001} Ni/Ni$_3$Al laminate composite, J. Mater. Res. Tech. 18 (2022) 4930–4945.

[44] R. Li, G. Wu, K. Liang, S.Z. Wang, L.H. Xue, Y.M. Sun, F. Dong, H. Li, S. Liu, Indenter radius effect on mechanical response of a-(11−20), c-(0001), and m-(−1100) plane GaN single crystals in nanoindentation: a molecular dynamics study, Mater. Sci. Semicond. Process. 145 (2022), 106648.

[45] P. Peng, G.L. Liao, T.L. Shi, Z.R. Tang, Y. Gao, Molecular dynamic simulations of nanoindentation in aluminum thin film on silicon substrate, Appl. Surf. Sci. 256 (2010) 6284–6290.

[46] Y.P. Yan, S.R. Zhou, S. Liu, Atomistic simulation on nanomechanical response of indented graphene/nickel system, Comput. Mater. Sci. 130 (2017) 16–20.

[47] A. Stukowski, Visualization and analysis of atomistic simulation data with OVITO–the open visualization tool, Model. Simul. Mater. Sci. Eng. 18 (2009), 015012.

[48] M. Novelli, P. Bocher, T. Grosdidier, Effect of cryogenic temperatures and processing parameters on gradient-structure of a stainless steel treated by ultrasonic surface mechanical attrition treatment, Mater. Charact. 139 (2018) 197–207.

[49] Y.L. Chiu, A.H.W. Ngan, Time-dependent characteristics of incipient plasticity in nanoindentation of a Ni$_3$Al single crystal, Acta Mater. 50 (2002) 1599–1611.

[50] R. Seymour, A. Hemeryck, K. Nomura, W.Q. Wang, R.K. Kalia, A. Nakano, P. Vashishta, Nanoindentation of NiAl and Ni$_3$Al crystals on (100), (110), and (111) surfaces: a molecular dynamics study, Appl. Phys. Lett. 104 (2014), 141904.

[51] W. Wang, C.B. Jiang, K. Lu, Deformation behavior of Ni3Al single crystals during nanoindentation, Acta Mater. 51 (2003) 6169–6180.

[52] W.D. Nix, H.J. Gao, Indentation size effects in crystalline materials: a law for strain gradient plasticity, J. Mech. Phys. Solids. 46 (1998) 411–425.

[53] G.M. Pharr, E.G. Herbert, Y. Gao, The indentation size effect: a critical examination of experimental observations and mechanistic interpretations, Annu. Rev. Mater. Res. 40 (2010) 271–292.

[54] S. Shim, H. Bei, E.P. George, G.M. Pharr, A different type of indentation size effect, Scr. Mater. 59 (2008) 1095–1098.

[55] K.K. Fung, N. Wang, I.K. Sou, Direct observation of stacking fault tetrahedra in ZnSe/GaAs(001) pseudomorphic epilayers by weak beam dark-field transmission electron microscopy, Appl. Phys. Lett. 71 (1997) 1225.

[56] S. Terayama, Y. Iwase, S. Hayakawa, T. Okita, M. Itakura, K. Suzuki, Molecular dynamic simulations evaluating the effect of the stacking fault energy on defect formations in face-centered cubic metals subjected to high-energy particle irradiation, Comput. Mater. Sci. 195 (2021), 110479.

[57] O.T. Kingstedt, J.T. Lloyd, On the conversion of plastic work to heat in mg alloy AZ31B for dislocation slip and twinning deformation, Mech. Mater. 134 (2019) 176–184.

[58] X.H. Luan, H.B. Qin, F.M. Liu, Z.B. Dai, Y.Y. Yi, Q. Li, The mechanical properties and elastic anisotropies of cubic Ni$_3$Al from first principles calculations, Crystals. 8 (2018) 307.

[59] J.E. Angelo, N.R. Moody, M.I. Baskes, Trapping of hydrogen to lattice defects in nickel, Model. Simul. Mater. Sci. Eng. 3 (1995) 289–307.

[60] R. Yang, Q. Zhang, P. Xiao, J. Wang, Y.L. Bai, Two opposite size effects of hardness at real nano-scale and their distinct origins, Sci. Rep. 7 (2017) 16053.

[61] T. Zhu, J. Li, A. Samanta, A. Leach, A. Gall, Temperature and strain-rate dependence of surface dislocation nucleation, Phys. Rev. Lett. 100 (2008), 025502.

[62] P. Li, X.G. Wang, Y.Z. Zhou, J. Pfetzing-Micklich, C. Somsen, G. Eggeler, Effect of aspect ratio on the deformation behavior of dislocation-free Ni$_3$Al Nanocubes, Nanomaterials 10 (2020) 2230.

[63] W. Wang, K. Lu, Nanoindentation measurement of hardness and modulus anisotropy in Ni$_3$Al single crystals, J. Mater. Res. 17 (2002) 2314–2320.

[64] F. Javaid, E. Bruder, K. Durst, Indentation size effect and dislocation structure evolution in (001) oriented SrTiO$_3$ Berkovich indentations: HR-EBSD and etch-pit analysis, Acta Mater. 139 (2017) 1–10.